Title

Translation of Ligand-Centered Hydrogen Evolution Reaction Activity and Mechanism of a Rhenium-Thiolate from Solution to Modified Electrodes: A Combined Experimental and Density Functional Theory Study

Journal

Inorganic Chemistry, 56(4)

ISSN

0020-1669

Authors

Zhang, Wuyu
Haddad, Andrew Z
Garabato, Brady D
et al.

Publication Date

2017-02-20

DOI

10.1021/acs.inorgchem.6b02829

Peer reviewed

Inorganic Chemistry

Article

pubs.acs.org/IC

Translation of Ligand-Centered Hydrogen Evolution Reaction Activity and Mechanism of a Rhenium-Thiolate from Solution to Modified Electrodes: A Combined Experimental and Density Functional Theory Study

Wuyu Zhang,[†,⊥] Andrew Z. Haddad,[†,⊥] Brady D. Garabato,[†] Pawel M. Kozlowski,[†,‡] Robert M. Buchanan,*[,†] and Craig A. Grapperhaus*[,†]

[†]Department of Chemistry, University of Louisville, 2320 South Brook Street, Louisville, Kentucky 40292, United States

[‡]Visiting Professor, Department of Food Sciences, Medical University of Gdansk, Al. Gen. J. Hallera 107, 80-416 Gdansk, Poland

Supporting Information

ABSTRACT: The homogeneous, nonaqueous catalytic activity of the rhenium-thiolate complex ReL_3 (L = diphenylphosphinobenzenethiolate) for the hydrogen evolution reaction (HER) has been transferred from nonaqueous homogeneous to aqueous heterogeneous conditions by immobilization on a glassy carbon electrode surface. A series of modified electrodes based on ReL_3 and its oxidized precursor $[ReL_3][PF_6]$ were fabricated by drop-cast methods, yielding catalytically active species with HER overpotentials for a current density of 10 mA/cm^2, ranging from 357 to 919 mV. The overpotential correlates with film resistance as measured by electrochemical impedance spectroscopy and film morphology as determined by scanning and transmission electron microscopy. The lowest overpotential was for films based on the ionic $[ReL_3][PF_6]$ precursor with the inclusion of carbon black. Stability measurements indicate a 2 to 3 h conditioning period in which the overpotential increases, after which no change in activity is observed within 24 h or upon reimmersion in fresh aqueous, acidic solution. Electronic spectroscopy results are consistent with ReL_3 as the active species on the electrode surface; however, the presence of an undetected quantity of catalytically active degradation species cannot be excluded. The HER mechanism was evaluated by Tafel slope analysis, which is consistent with a novel Volmer–Heyrovsky–Tafel-like mechanism that parallels the proposed homogeneous HER pathway. Proposed mechanisms involving traditional metal-hydride processes vs ligand-centered reactivity were examined by density functional theory, including identification and characterization of relevant transition states. The ligand-centered path is energetically favored with protonation of cis-sulfur sites culminating in homolytic S–H bond cleavage with H_2 evolution via H atom coupling.

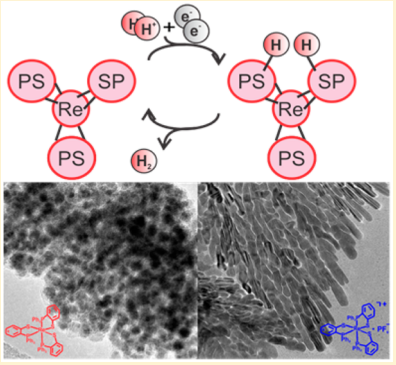

INTRODUCTION

Use of hydrogen as an energy carrier offers a potential carbon-free alternative to fossil fuels.[1] Estimates suggest a hydrogen-based economy would require as much as 150 million tons of H_2 annually,[2] fueling the need for efficient electrolytic and/or photochemical catalysts.[3] Development of heterogeneous and homogeneous catalysts for the hydrogen evolution reaction (HER), $2H^+ + 2e^- \rightarrow H_2$, and the hydrogen oxidation reaction (HOR), its reverse, has received significant attention.[4−15] The ideal catalyst is Pt; however, its application in large-scale hydrogen production is limited by the its cost and scarcity.[16] This has prompted the development of new earth-abundant electrocatalysts, including transition-metal phosphides,[17,18] selenides,[19] and sulfides. Molybdenum sulfides have shown great promise as an economical alternative to Pt.[20−22] The high activity of MoS_2 arises in large part from the location and number of cis-sulfur edge sites.[22]

Recently, we reported the homogeneous electrocatalytic HER/HOR activity of ReL_3 (L = diphenylphosphinobenzenethiolate).[6] The ReL_3 complex contains three thiolate donors with cis-thiolates similar to the S edges of MoS_2. The HER mechanism of ReL_3 is proposed to follow a unique ligand-centered mechanism that avoids metal hydrides.[6] This reactivity deviates from most homogeneous systems which operate via crucial metal-hydride intermediates, with several displaying low overpotentials, high turnover frequencies, and faradaic efficiencies >90%.[5,11] The ReL_3 system is one of only a few examples of ligand-centered HER/HOR reactions reported to date[6,23−27] as well as one of the only ligand-centered homogeneous systems employing a cis-sulfur active site, affording a unique opportunity to correlate ligand-centered homogeneous catalytic and mechanistic studies with heterogeneous studies.

The current study involves fabrication of surface modified electrodes through simple physisorption, which avoids

Received: November 27, 2016
Published: February 9, 2017

DOI: 10.1021/acs.inorgchem.6b02829
Inorg. Chem. 2017, 56, 2177−2187

modification of the molecular ReL_3 catalyst while retaining solution HER activity of ReL_3. This approach has previously been employed for other HER catalysts.[28−33] Notable examples include Fontecave and co-worker's multiwalled carbon nanotube $[Ni(P^{Ph}_2N^{Ph}_2)_2]$ modified electrodes, which display high catalytic activity for both HER and HOR in acetonitrile.[28] Pantani and co-workers observed HER activity with Co-$(dmgBF_2)_2(CH_3CN)_2$/carbon black (CB)/Nafion coated glassy carbon (GC) electrodes,[29] while Peters and co-workers modified GC electrodes with cobaloximes as HER catalysts with low overpotentials in aqueous solutions (pH < 4.5).[29,30] Other electrode surfaces modified with cobalt porphyrin,[34] metal-phthalocyanine,[35−38] and an organometallic Rh complex incorporated in a Nafion film[39] have also been reported as HER electrocatalysts but at higher overpotentials.

To this end, we translated the homogeneous HER activity of ReL3 in nonaqueous solution to a series of four modified GC electrodes (Scheme 1) for heterogeneous application in an acidic aqueous environment along with density functional theory (DFT) computations which confirm the ligand-centered HER mechanism. Additionally, we followed a recent protocol by Jaramillo and co-workers for benchmarking the efficiency and long-term stability of HER electrocatalysts.[23]

Scheme 1. Schematic of ReL_3 Modified Electrodes

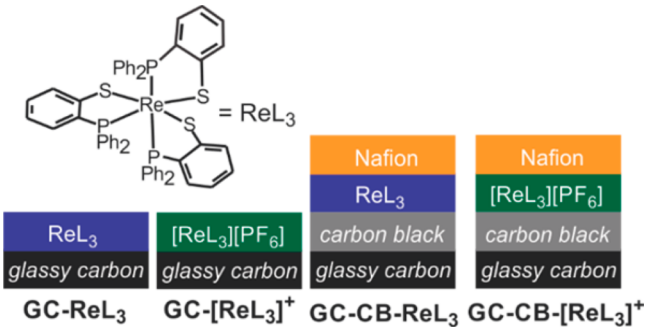

EXPERIMENTAL SECTION

Materials and Reagents. Chemicals and reagents were purchased from commercial sources and used without further purification unless otherwise noted. Carbon black was purchased from Columbian Chemicals Company (Marietta, GA). All solvents were purified using an MBraun solvent purification system prior to use. The catalyst ReL_3[40] and the catalyst precursor $[ReL_3][PF_6]$[41] were prepared according to previously reported literature methods.

Electrode Fabrication. GC electrodes of model number MF-2012 with a 3.0 mm diameter were purchased from Bioanalytical Systems Inc. (West Lafayette, IN). Electrodes were polished with alumina slurry (0.5 μm) before use and then sonicated in acetone, isopropanol, and deionized water for 15 min, separately.

GC-ReL_3 Electrodes. Catalyst solutions for ReL_3 were typically prepared by dissolving 3.0 mg (2.5×10^{-3} mmol) of ReL_3 in 1.00 mL of dichloromethane (DCM). Aliquots of the catalyst solution were then carefully drop-cast onto the clean glassy carbon electrodes (area = 0.071 cm^2) using a micropipette, ensuring that all of the solution remained on the electrode until evaporation. Loading amounts ranged from 10 to 160 nmol of catalyst. Optimal loading conditions were determined by voltammetric methods. The GC-ReL_3 electrodes were stored open to air prior to use.

GC-$[ReL_3]^+$ Electrodes. The GC-$[ReL_3]^+$ electrodes were prepared in an argon filled glovebox from a freshly prepared stock solution of 2.5 mM $[ReL_3]PF_6$ in dry, degassed DCM. The drop-casting method, catalyst loadings, and optimization procedure were the same as that described for GC-ReL_3. The GC-$[ReL_3]^+$ electrodes were stored open to air.

GC-CB-[ReL_3] and GC-CB-$[ReL_3]^+$. The CB modified electrodes GC-CB-$[ReL_3]$ and GC-CB-$[ReL_3]^+$ were prepared as follows. A 1.0 mg portion of CB was added to 1.0 mL of dimethylformamide (DMF), and the mixture was sonicated for 30 min. Then, 12 μL of the CB solution was transferred to the surface of a clean GC electrode and heated under an infrared heating lamp for ~15 min to evaporate the solvent. The resulting CB film evenly covered the electrode surface. Next, 60 nmol of either ReL_3 or $[ReL_3][PF_6]$ was carefully deposited on top of the CB layer by drop-casting of DCM solutions as noted above. After evaporation of the solvent, a 5.0 μL portion of a 5.0% w/w Nafion solution was added via micropipette. The electrode was dried under an infrared heating lamp. Electrodes were stored in air prior to use.

Physical Methods. Voltammetry and coulometry measurements were performed using a Gamry Interface 1000 potentiostat with a three-electrode cell employing a $[ReL_3]^{n+}$ (n = 0 or 1) modified GC electrode as the working electrode, a platinum wire as the counter electrode, and Ag/AgCl saturated in 3.5 M KCl as the reference electrode. For all of the measurements, the sample was purged for 15 min with N_2 and then kept under an N_2 atmosphere. Polarization curves and electrochemical impedance spectra (EIS) were collected on a CHI 660 electrochemical workstation. All reported potentials are scaled versus the reversible hydrogen electrode (RHE) according to eq 1 using a value of +0.205 V for $E^\circ_{Ag/AgCl}$.

$$E_{RHE} = E_{Ag/AgCl} + 0.059\ pH + E^\circ_{Ag/AgCl} \quad (1)$$

Scanning electron microscopy (SEM) images were obtained using a LEO 1550 field emission SEM. Transmission electron microscopy (TEM) images were generated using a FEI Tecnai F20 electron microscope operating at 200 kV. UV−vis absorbance spectra were recorded on a UV-3600 Shimadzu UV−vis−near infrared (NIR) spectrophotometer. A Gow-Mac series 400 GC-TCD with a molecular sieve column was used to identify the hydrogen gas that was generated after electrolysis. The column was heated to 130 °C under N_2 gas flow, and 250 μL samples were drawn from the headspace of the electrolysis cell and then injected into the column using a gastight syringe.

Electrocatalytic HER Measurements. Cyclic voltammetric (CV) measurements were carried out at room temperature in 0.5 M H_2SO_4 at a scan rate of 200 mV/s. Current densities were normalized based on the surface area (0.071 cm^2) of the GC electrode. Polarization data were collected under the same conditions but at a scan rate of 20 mV/s. Initial evaluation of electrode stability was conducted by continuous scanning over 500 CV cycles. Extended stability was assessed by recording the required overpotential to maintain a current density of 10 mA/cm^2 over a 24 h period. To determine Faradaic efficiency, the reaction was conducted in a H cell that separated the anode and cathode. The volume of H_2 gas collected above the cathode was quantified and compared to the measured charge.

Electrochemical Impedance Spectroscopy Methods. EIS was measured over a frequency range from 10^{-2} to 10^5 Hz under an amplitude of 10 mV. Nyquist curves were recorded for the HER processes. The experimental complex-plane plots for GC-$[ReL_3]^{n+}$ (n = 0 or 1) and GC-CB-$[ReL_3]^{n+}$ (n = 0 or 1) were recorded at an applied overpotential of 1.3 V (see Supporting Information). Data were fit to a model (Figure 1) with a resistor (R_s) in series with a module comprised of a second resistor (R_{ct}) in parallel with a constant phase element (CPE), where R_s represent the contact resistance between electrolyte and electrode surface, R_{ct} represents the charge

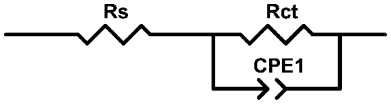

Figure 1. Electrical equivalent circuit model for EIS data interpretation for the ReL_3 modified GC electrodes.

DOI: 10.1021/acs.inorgchem.6b02829
Inorg. Chem. 2017, 56, 2177−2187

transfer resistance within the catalyst film, and CPE is a constant phase element[42] representing the capacitive behavior of the electrodes.

Computational Methods. All reported calculations were performed in the gas phase using DFT employing the M06 exchange correlation functional[43] and the LANL2DZ basis set for all atoms, as implemented in the Gaussian09 suite of programs.[44] Initially, the restricted formalism using an RHF wave function was invoked, and subsequently unrestricted calculations based on a UHF-type wave function were carried out for complexes with even electron counts. Furthermore, the B3LYP functional was used to obtain broken symmetry solutions.[45−49] Frequency calculations were performed for all optimized stationary points to ensure they were true minima. Transition states (TS) were determined using the Berny algorithm with GEDIIS and verified by intrinsic reaction coordinate (IRC) calculations with forward and reverse step sizes of 40. TS structures were constructed manually based on their optimized reactants and products under tight constraints with no symmetry imposed. Chemcraft software was used for graphics visualization.[50]

RESULTS AND DISCUSSION

Electrode Modification. A series of four modified GC electrodes were prepared based on the homogeneous HER catalysts ReL_3 (Scheme 1). The ReL_3 complex and its oxidized derivative $[ReL_3][PF_6]$ are readily soluble in DCM but insoluble under aqueous conditions, attributable to the large number of phenyl rings in the structure. As such, evaporation of dichloromethane solutions of ReL_3 or $[ReL_3][PF_6]$ on GC surfaces yield water-stable films due to adhesive dispersion forces and/or ion-induced dipole interactions. Once prepared, all modified electrodes were stable under ambient conditions and upon submersion in aqueous solution over a pH range of 0.25−13 as determined by voltammetry over a period of several days.

The simplest electrode, GC-ReL_3, consists of a GC surface coated with an electroactive film of ReL_3. The film was fabricated by drop-casting a controlled volume of a 2.5 M DCM solution of ReL_3, which leaves a known molar quantity of catalyst on the electrode upon solvent evaporation. Similar methodology was employed to prepare GC-$[ReL_3]^+$, which has a film of formal Re(II) catalyst precursor $[ReL_3][PF_6]$. A key difference between GC-ReL_3 and GC-$[ReL_3]^+$ is that the former has a charge neutral catalyst film, while the latter has an ionic catalyst film. Diffuse reflectance spectra confirm the presence of ReL_3 (544 nm) and $[ReL_3]^+$ (580 nm) on the surface of GC-ReL_3 and GC-$[ReL_3]^+$, respectively.[51]

Multilayer modified electrodes GC-CB-ReL_3 and GC-CB-$[ReL_3]^+$ were prepared to enhance conductivity and promote substrate binding. These electrodes consist of a GC surface with an initial CB layer, followed by a catalyst film of ReL_3 or $[ReL_3][PF_6]$ and topped with a layer of Nafion. The CB, added to improve conductivity between the GC surface and the catalyst,[52] was drop-cast as a DMF slurry followed by drying upon an infrared heat lamp. After incorporation of the catalyst film, addition of the ionic polymer Nafion to promote film stability and proton binding was done by drop-casting an aqueous Nafion solution with further drying under the heat lamp.

Electrocatalytic HER. As previously reported, ReL_3 is an effective homogeneous HER electrocatalyst in dichloromethane solution with a maximum turnover frequency of $32 \pm 3\ s^{-1}$.[6] To evaluate the HER activity of ReL_3 under heterogeneous aqueous conditions, polarization curves were recorded for the modified electrodes in 0.5 M H_2SO_4 under ambient conditions (Figure 2). Results are summarized in Table 1, which compares

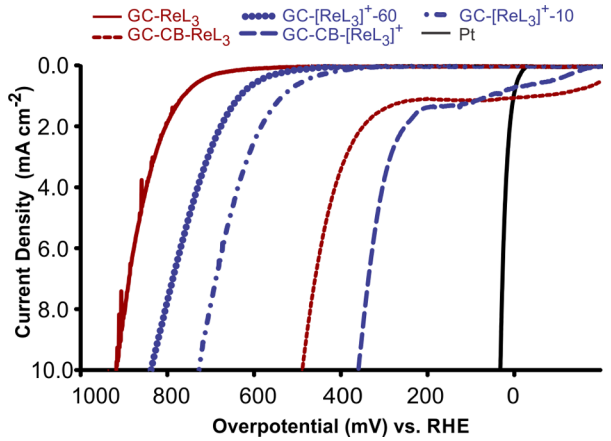

Figure 2. Polarization curves of GC-$[ReL_3]^{n+}$ and GC-CB-$[ReL_3]^{n+}$ (n = 0 and 1) recorded in 0.5 M $H_2SO_{4(aq)}$ with the modified electrode as the working electrode, a Pt wire as the counter electrode, and Ag/AgCl (3.5 M KCl) as the reference.

Table 1. HER Overpotentials (η) and Tafel Slopes of the ReL_3 Modified Electrodes

electrode	loading (nmol)	η^a (mV)	Tafel slope (mV/dec)
GC-ReL_3	60	919	154
GC-$[ReL_3]^+$	60	835	175
GC-$[ReL_3]^+$	10	727	190
GC-CB-ReL_3	60	487	199
GC-CB-$[ReL_3]^+$	60	357	155

^{a}Converted to RHE from values measured versus Ag/AgCl using $E_{RHE} = E_{Ag/AgCl} + 0.059\ pH + 0.205$ V.

the overpotential required to obtain a current density of 10 mA/cm^2 for the 4 electrodes at 60 nmol catalyst loading. The charge neutral film of GC-ReL_3 exhibits the largest overpotential of 0.919 V, whereas incorporation of the ionic, oxidized catalyst precursor $[ReL_3]^+$ lowers the overpotential of GC-$[ReL_3]^+$ by as much as 0.192 V. Notably, the optimized loading of GC-$[ReL_3]^+$ (10 nmol catalyst) is substantially lower than that of GC-ReL_3 (60 nmol catalyst). Overpotential decreases by an additional 0.43−0.47 V in the multilayered electrodes. Thus, overpotentials as low as 0.357 V are observed for GC-CB-$[ReL_3]^+$, which is 0.290 V lower than cobaloxime modified GC electrodes.[30] As detailed below, the overpotential of ReL_3 modified electrodes correlates with film morphology and resistance.

To evaluate the Faradaic efficiency, controlled potential coulometry at −1.48 V versus RHE was applied for a fixed time. Electrolysis was performed in a two-compartment cell with the evolved H_2 collected in the headspace above the cathode. To calculate the Faradaic efficiency, the molar quantity of H_2 as determined from the volume of the collected gas and compared to the quantity of charge passed. Faradaic efficiencies of GC-$[ReL_3]$ and GC-$[ReL_3]^+$ were calculated as 97 and 98%, respectively, over 160 s. For the CB modified electrodes, Faradaic efficiencies of 87 and 90% were measured for GC-CB-$[ReL_3]$ and GC-CB-$[ReL_3]^+$, respectively, over 100 s.

Electrode Stability. Initial assessment of the electrode stability of GC-$[ReL_3]$ and GC-$[ReL_3]^+$ was conducted by CV. Continuous scanning over 500 cycles ranging from +0.32 to −1.48 V versus RHE at a scan rate of 200 mV/s resulted in an increase of overpotential by 300 and 350 mV for GC-$[ReL_3]$ and GC-$[ReL_3]^+$, respectively (see Supporting Information).

DOI: 10.1021/acs.inorgchem.6b02829
Inorg. Chem. 2017, 56, 2177−2187

The long-term stability of GC-$[ReL_3]^{n+}$ (n = 0 or 1) was benchmarked through chronopoteniometry at a fixed catalytic current density of 10 mA/cm^2 over 24 h. For GC-$[ReL_3]$, the overpotential increases by 510 mV over the first 3 h but then remains constant over the remainder of the experiment, consistent with initial conditioning of the electrode. For GC-$[ReL_3]^+$, the increase in overpotential is slightly less, 430 mV, over the first 2 h with a good stability for the remainder of the experiment (see Supporting Information). The initial increase in overpotential can be attributed to a decrease in the number of active sites on the surface (see Figure S4), which would increase the potential required to maintain the same current density. For both GC-$[ReL_3]$ and GC-$[ReL_3]^+$, no further change in overpotential was observed upon placing the conditioned electrode in a fresh 0.5 M H_2SO_4 solution and applying a potential.

The stability of CB modified electrodes was similarly evaluated. The initial CV studies revealed an increase in overpotential of 340 and 400 mV for GC-CB-$[ReL_3]$ and GC-CB-$[ReL_3]^+$, respectively, after 500 cycles. Chronopotentiometry measurements of GC-CB-$[ReL_3]$ required an increase in overpotential of 1.0 V during the first 1.5 h to maintain a current density of 10 mA/cm^2. Notably, the final overpotential of 1.53 V is statistically equivalent to the value observed for GC-$[ReL_3]$, indicating that the benefits of CB do not persist over prolonged electrolysis. The GC-CB-$[ReL_3]^+$ electrodes behave similarly with an increase in overpotential of 1.0 V to a final value consistent with GC-$[ReL_3]^+$.

Microscopy Studies. Microscopy studies reveal distinct differences in the morphology of the charge neutral film of GC-ReL_3 and the ionic film of GC-$[ReL_3]^+$. The SEM image of GC-ReL_3 (Figure 3a) shows a porous multilayer structure distributed with uneven surface coverage. This is consistent with a preference for cohesive interactions between ReL_3 molecules over adhesive interactions between ReL_3 and the GC surface. The TEM image (Figure 3b) reveals that the ReL_3 film is comprised of randomly arranged plate-shaped nanoparticles approximately 10 nm in diameter. In contrast, the SEM image of GC-$[ReL_3]^+$ (Figure 3c) displays more highly uniform film coverage, although substantial cracking is evident. The uniformity is attributed to stronger adhesive interactions between the complex ions and the GC surface. The TEM image of the $[ReL_3]^+$ film (Figure 3d) finds larger dendritic shaped nanoparticles aligned in two dimensions.

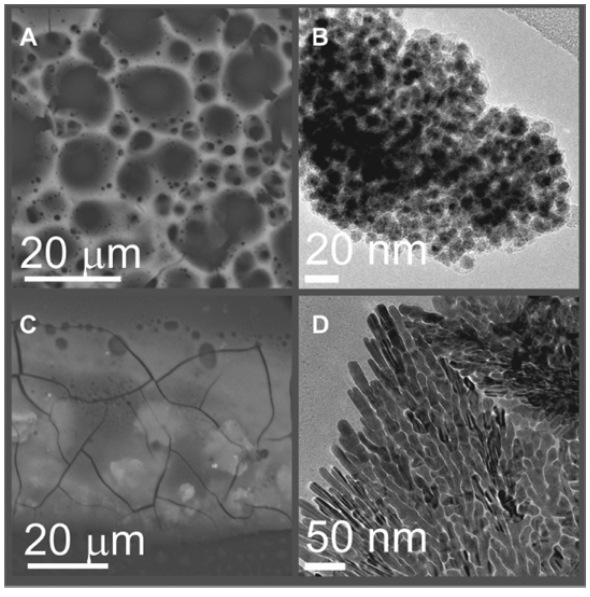

Figure 3. Film topography prior to HER. SEM images of GC-ReL_3 (A) and GC-$[ReL_3]^+$ (C) films and TEM images of ReL_3 (B) and $[ReL_3]^+$ (D) films.

The differences in film morphology correlate with the optimal catalyst loading. For GC-ReL_3, catalytic current steadily increases upon addition of catalyst up to 60 nmol as the porous structure of small nanoplates provides a pathway for substrate/electrolyte transfer deeper into the film. In contrast, the uniform dendritic film of GC-$[ReL_3]^+$ displays optimal HER activity at lower loading (10 nmol). Decreased activity at higher loading suggests an increased charge transfer resistance through thicker layers as confirmed by electron impedance spectroscopy (Table 2). For GC-ReL_3 and GC-ReL_3^+, SEM images (Supporting Information) collected after H_2 evolution reveal film degradation.

Table 2. Simulated Nyquist Plot Parameters for ReL_3 Modified Electrodes from the Impedance Spectra at 1.0 V

electrode/load (nmol)	R_s (Ω)	R_{ct} (MΩ)	CPE-T (sP/μΩ)	CPE-P (sP/Ω)
GC-ReL_3/10	43.3	1.38	0.6	0.83
GC-ReL_3/60	41.1	0.72	2.0	0.88
GC-ReL_3/120	39.5	0.88	1.5	0.84
GC-$[ReL]_3^+$/10	19.5	0.09	0.2	0.84
GC-$[ReL]_3^+$/60	18.6	0.25	9.0	0.90
GC-$[ReL]_3^+$/120	19.5	0.87	2.0	0.80
GC-CB-$[ReL]_3$/60	31.3	0.006	170	0.79
GC-CB-$[ReL]_3^+$/60	50.0	0.004	240	0.70

Impedance Studies. Electrochemical impedance spectroscopy confirms a correlation between film resistance and HER overpotential. Data were collected over a frequency range of 10^{-2} to 10^5 Hz at an applied overpotential of 1.3 V. Nyquist plots of the EIS data (see Supporting Information) were simulated using the model in Figure 1. Simulation parameters are provided in Table 2. The similarity among the responses of all fabricated GC electrodes suggests a similar mechanism for hydrogen evolution, and the lack of Warburg impedance indicates that mass transport is rapid enough so that the reaction is kinetically controlled.[20]

The R_{ct} term, which represents charge transfer resistance within the catalyst film, has the largest impact on overpotential (Table 2). The multilayered modified electrodes require the least overpotential and also display the lowest R_{ct} with values of 0.004 and 0.006 MΩ for GC-CB-$[ReL_3]^+$ and GC-CB-ReL_3, respectively. The R_{ct} for the ionic film of GC-$[ReL_3]^+$ is 0.09 MΩ under optimal loading conditions, which is 24 times larger than that for GC-CB-$[ReL_3]^+$. Additional catalyst loading increases the R_{ct} of GC-$[ReL_3]^+$ consistent with slower electron transfer through the thicker film. The charge neutral catalyst film of GC-ReL_3 displays the largest R_{ct} of 0.72 MΩ under optimal loading conditions and also requires the largest overpotential.

Evaluation of Active Species. To investigate the identity of the active species on the electrode surface, a series of UV–visible studies was performed. First, to verify the presence of intact complex on the electrode surface, diffuse reflectance measurements of catalysts deposited on optically transparent indium tin oxide (ITO) electrodes were collected after initial

DOI: 10.1021/acs.inorgchem.6b02829
Inorg. Chem. 2017, 56, 2177–2187

deposition and following catalysis. The spectra (Figures 4a and b) confirm the presence of ReL_3 (544 nm) and $[ReL_3]^+$ (580

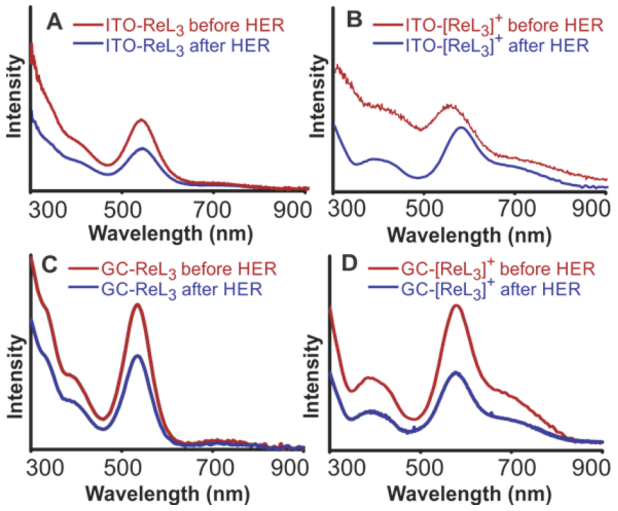

Figure 4. Diffuse reflectance spectra before and after HER catalysis of ITO-$[ReL_3]$ (a) and ITO-$[ReL_3]^+$ (b). Solution electronic spectra of DCM washings before and after HER catalysis of GC-$[ReL_3]$ (c) and GC-$[ReL_3]^+$ (d).

nm) on the surface of freshly prepared ITO-ReL_3 and ITO-$[ReL_3]^+$, respectively.[51] Following HER, both films display a peak at 544 nm, indicating that all surface exposed complex has been converted to the ReL_3 catalyst resting state. To evaluate if the bulk material has also been converted to ReL_3, the $[ReL_3]^{n+}$ film was removed from the GC electrode surface by washing with DCM, and UV−visible analysis of the resulting solution was performed. The spectra of DCM washings collected after HER at an applied potential of −1.48 V in 0.5 M H_2SO_4 for 3 min are identical to those collected prior to catalysis (Figures 4c and d). The results indicate the complexes are stable during catalysis with no formation of additional DCM soluble species. Further, the DCM rinsed electrodes are inactive for HER upon reimmersion into the H_2SO_4 solution, precluding the presence of a metal sulfide cluster or similar species on the GC surface or dispersion in the aqueous solution as the HER catalyst. The combined spectroscopic results convincingly establish intact $[ReL_3]^{n+}$ complexes on the modified GC electrodes. Because $[ReL_3]^{n+}$ is active for homogeneous HER, we attribute the heterogeneous HER activity to these surface confined $[ReL_3]^{n+}$ species but cannot exclude the possibility that activity could also result from an unobserved degradation product.

Tafel Slope Analysis. The Tafel plot for an HER displays the relationship between the applied overpotential and catalytic current density. The slope of the Tafel plot is dependent on the rate limiting step, and its value is commonly used to evaluate the mechanism of HER on metal surfaces under acidic conditions. The two dominant mechanisms for HER on metal surfaces are Volmer−Heyrovsky (eqs 2 and 3) and Volmer−Tafel (eqs 2 and 4).[53]

Volmer (discharge reaction):

$$H_3O^+ + e^- + cat \rightleftarrows cat - H + H_2O \quad (2)$$

Heyrovsky (ion + atom reaction):

$$H_3O^+ + e^- + cat - H \rightleftarrows cat + H_2 + H_2O \quad (3)$$

Tafel (combination reaction):

$$cat - H + cat - H \rightleftarrows 2cat + H_2 \quad (4)$$

Both mechanisms begin with a Volmer step, which is a discharge reaction that combines H^+ and an electron to yield a metal hydride (cat-H). In the Volmer−Heyrovsky mechanism, the second step is a Heyrovsky "ion + atom" reaction that releases H_2 following the addition of a second proton and electron to cat-H. Alternately, in a Volmer−Tafel mechanism, the second step is a Tafel combination reaction with H_2 release upon combination of two equivalents of cat-H. If the Volmer step is rate limiting, the theoretical Tafel slope is 116 mV/decade regardless of the identity of the subsequent step. However, if the Volmer step is fast, the Tafel slope is dependent on the second step. For a Volmer−Heyrovsky mechanism with a slow Heyrovsky step, a Tafel slope of 38 mV/decade is predicted, whereas a slope of 29 mV/decade is expected for a Volmer−Tafel mechanism with a slow Tafel step. Ideal Tafel slopes serve as benchmarks to assign the rate limiting HER step on metal surfaces, although actual values may deviate.[20,53,54]

Although Tafel slope interpretations were developed for HER at metal surfaces, they have been applied to evaluate the mechanism of other heterogeneous catalysts such as molybdenum sulfides[20,21] that are deposited on electrode surfaces. Tafel analyses of the HER polarization curves of the $[ReL_3]^{n+}$ modified electrodes (Figure 5) reveal slopes from 139

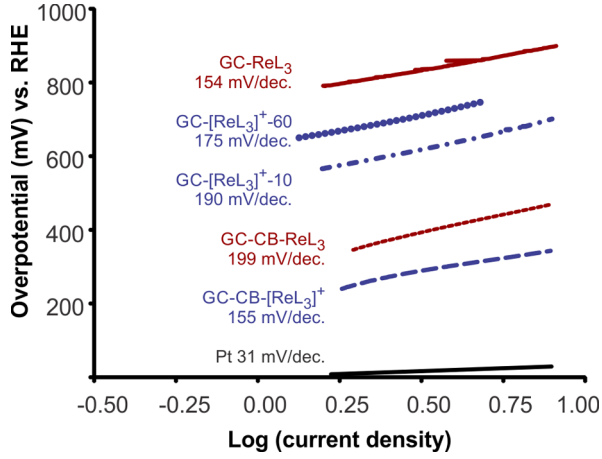

Figure 5. Tafel slope plots for GC-$[ReL_3]^{n+}$ and GC-CB-$[ReL_3]^{n+}$ (n = 0 or 1).

to 193 mV/decade (Table 1). The slopes did not significantly change for data collected using a rotating disk electrode at variable rotation speeds (see Supporting Information). The slopes are considerably greater than the 31 mV/decade observed for Pt but consistent with the proposed HER mechanism for ReL_3 complexes in homogeneous solution (Scheme 2).

The proposed homogeneous HER mechanism for ReL_3 (Scheme 2) correlates with the proposed heterogeneous HER mechanism of the ReL_3 modified electrodes (Scheme 3). The "like" term signifies that the steps on the modified surface resemble those on traditional heterogeneous metal surfaces with the notable exception that all bond-making and bond-breaking occurs at the sulfur ligands of a single metal site. That is, immobilization of ReL_3 on GC translates both the HER activity and the HER mechanism from homogeneous to

DOI: 10.1021/acs.inorgchem.6b02829
Inorg. Chem. 2017, 56, 2177−2187

Scheme 2. Proposed Homogeneous HER Mechanism for ReL_3 Highlighting Re-Dithiol vs Re-Hydride Isomers as the Key Intermediates

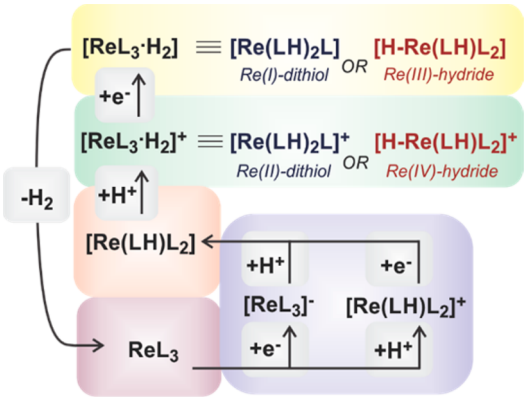

Scheme 3. Proposed Volmer–Heyrovsky–Tafel-like Mechanism for Heterogeneous HER ReL_3 Modified Electrodes[a]

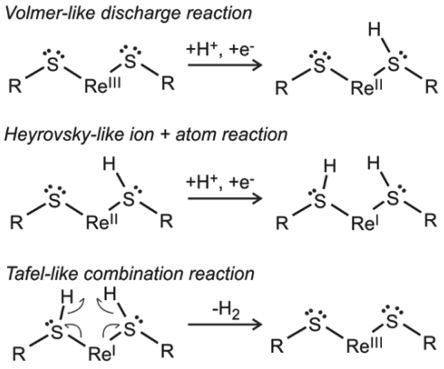

[a]For simplicity, only the Re-$(SR)_2$ portion of the catalyst is shown.

heterogeneous conditions. The large Tafel slopes for the ReL_3 modified electrodes suggest a rate limiting Volmer-like step, which corresponds with initial thiolate protonation and complex reduction. The second step is described as a Heyrovsky-like step, as it involves the reaction of the second proton and electron at the initial active site to yield the formal Re^{I}-dithiol $Re(LH)_2L$. This is distinct from a second Volmer step, which would involve proton/electron addition at a second reactive site (see Supporting Information for a detailed description). The final H_2 evolution step involves homolytic S–H bond cleavage of the cis-thiols similar to the coupling of metal hydrides in a Tafel step. The similarity of the homogeneous and heterogeneous mechanisms derives from the fact ReL_3 serves as the active catalyst under both conditions. For the ReL_3 modified electrodes, the electrode surface provides reducing equivalents without significantly altering ReL_3 reactivity. The proposed mechanisms are supported by density functional theory computations.

DFT Studies. To elucidate the mechanism of hydrogen evolution by discrete ReL_3 active sites, DFT calculations were performed. These gas phase calculations are representative of the single site activity under homogeneous and surface confined conditions. The electronic and geometric properties of all complexes of the proposed mechanism in Scheme 2 were explored along with location of their transition states for H_2 evolution pathways. Complexes with an even number of electrons (ReL_3, $[Re(LH)L_2]^+$, $[HRe(LH)L_2]$, and $[Re(LH)_2L]$) were considered in both the singlet ($S = 0$) and triplet ($S = 1$) ground states for both closed-shell and open-shell configurations. All odd electron complexes ($[ReL_3]^-$, $[Re(LH)L_2]^0$, and $[Re(LH)_2L]^+$) were calculated as doublets ($S = {}^1/_2$). Intermediates formed upon the addition of one proton were evaluated with protonation at S3, consistent with previous X-ray crystallographic studies.[40] Addition of the second proton was examined for both ligand-based protonation at S2 and metal-based addition as the Re-hydride.

The ground state of the neutral ReL_3 complex is best described as a restricted singlet Re(III) (d^4, $S = 0$) center bound to three thiolate ligands (Figure 6). Optimized metal–

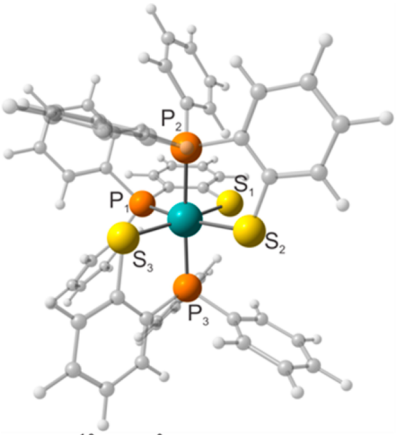

$^{1,3}[ReL_3]^0$ ΔG = 0.0 / +2.6

	S = 0 / S =1	Exp.
Re-S1	2.57 / 2.42	2.477(5)
Re-S2	2.36 / 2.45	2.303(5)
Re-S3	2.35 / 2.49	2.269(5)
Re-P1	2.52 / 2.48	2.473(5)
Re-P2	2.46 / 2.59	2.391(5)
Re-P3	2.43 / 2.50	2.411(5)
P2-Re-P3	166.6 / 170.8	166.7(1)

Figure 6. Bond lengths (Å) and angles (deg) for ReL_3 from $S = 0$ and $S = 1$ DFT optimizations (M06/LANL2DZ) and the experimental (Exp.) X-ray crystal structure.[40] ΔG indicates relative zero-point free energy (kcal/mol) values of the $S = 0$ and $S = 1$ electronic states.

ligand bond lengths for the singlet ground state are 0.02–0.09 Å longer than experimental values, as typical for DFT calculations, while triplet state deviations from experimental bond lengths were larger. Furthermore, the neutral singlet species ($S = 0$) was favored over the triplet state ($S = 1$) by 2.6 kcal/mol. Due to the small difference in energy between the singlet and triplet states, attempts were made to obtain broken symmetry solution for the open-shell singlet. Calculations for the open-shell singlet were performed using the singlet geometry in combination with triplet orbitals as initial guesses. Examination of optimization steps show a decrease in the ⟨S**2⟩ value moving from 2.0152 and collapsing to a final value of 0.00. This result confirms the nature of the ReL_3 complex as a closed-shell restricted singlet.

The initial steps of the catalytic mechanism involve the transfer of one proton and one electron to ReL_3 to yield the neutral $[Re(LH)L_2]$ intermediate. Prior studies indicate that either proton or electron transfer can occur first.[6] Initial protonation at S3 yields the previously isolated and characterized $[Re(LH)L_2]^+$. The $[Re(LH)L_2]^+$ intermediate is best described as a Re(III) ($S = 1$) open-shell triplet coordinated by two noninnocent thiolate donors and one

DOI: 10.1021/acs.inorgchem.6b02829
Inorg. Chem. 2017, 56, 2177–2187

thiol donor (Figure 7). Single-point energy calculations were performed as both closed-shell singlet and triplet in addition to obtaining the broken symmetry solution. Comparison of the triplet state geometric parameters reveal good agreement with the X-ray crystal structures of $[Re(LH)L_2]^+$. The free energy of the triplet is also preferred energetically, lying 5.33 kcal/mol lower than the closed-shell singlet and 3.55 kcal/mol lower than the open-shell singlet. Further examination of the ⟨S**2⟩ values confirms an open-shell configuration of the triplet, yielding a final value of 2.0132 with the less energetically preferred open-shell singlet with an ⟨S**2⟩ value of 0.9516.

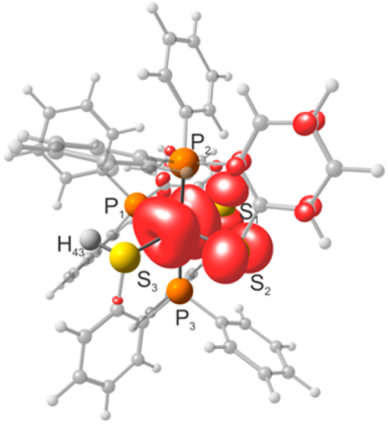

$^{1,3}[Re(LH)L_2]^+$ ΔG = +5.33 / 0.0

	S = 0 / S =1	Exp.
Re-S1	2.37 / 2.39	2.3575(6)
Re-S2	2.37 / 2.42	2.2884(6)
Re-S3	2.51 / 2.58	2.2875(6)
Re-P1	2.54 / 2.50	2.4976(6)
Re-P2	2.51 / 2.44	2.4493(6)
Re-P3	2.49 / 2.50	2.4419(6)
S3-H43	1.38 / 1.38	1.077(18)
P2-Re-P3	166.6 / 166.5	166.7(1)

Figure 7. Bond lengths (Å) and angles (deg) for $[Re(LH)L_2]^+$ from *S* = 0 and *S* = 1 DFT optimizations (B3LYP/LANL2DZ) and the experimental (Exp.) X-ray crystal structure.[6] Δ*G* indicates relative zero-point free energy (kcal/mol) values of the *S* = 0 and *S* = 1 electronic states.

For the double intermediates $[ReL_3]^-$, $[Re(LH)L_2]^0$, and $[Re(LH)_2L]^+$, examination of the atomic spin densities (SD) reveals a propagation of ligand-centered radical character around the three S donors with each protonation step. The formal Re(II) species $[ReL_3]^-$ shows 6.5 and 6.4% SD on the S2 and S3 donors, respectively, with no significant contribution from S1 (Figure 8). This suggests S2 and S3 have a small degree of thiyl character and can be considered "noninnocent", while S1 is best described a thiolate. Protonation of $[ReL_3]^-$ occurs preferentially at S3, yielding $[Re(LH)L_2]$ and resulting in a notable transfer of spin-density from S3 and Re onto S1 and S2. The S1 and S2 donors are now noninnocent with 8.6 and 9.1% SD, respectively, whereas S3 is a thiol (Figure 8). The next step of the mechanism is the formation of $[Re(LH)_2L]^+$ upon addition of the second proton. Although this may potentially occur at sulfur, yielding a Re(II)-dithiol or at the metal to give a Re(IV)-hydride, only the former structure could be optimized. Protonation is favored at S2, prompting a shift of SD onto S1, which now accounts for 23.1% of the unpaired SD (Figure 8). The electronic structure of $[Re(LH)_2L]^+$ is doublet ($S = {}^1/_2$) with a formal Re(II) center coordinated by a noninnocent thiolate (S1) and two thiols (S2 and S3).

Propagation of spin density as a function of protonation may be seen by analyzing the geometric parameters of the doublet intermediates. The Re−S1 bond distance decreases as a function of ligand electron density, further indicating non-

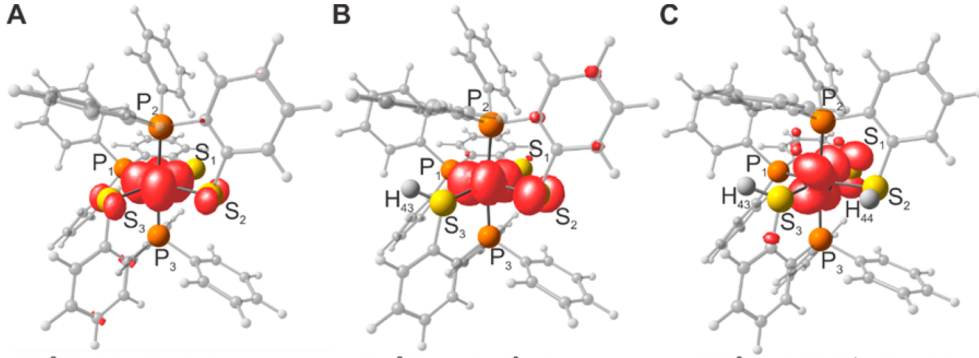

(A) $^2[ReL_3]^-$ ΔG = 0.0

S = 1/2	
Re-S1	2.57
Re-S2	2.47
Re-S3	2.46
Re-P1	2.45
Re-P2	2.42
Re-P3	2.41
S3-H43	N/A
S2-H44	N/A
P2-Re-P3	168.2

(A) Atom SD %
S1 = 0
S2 = 6.5
S3 = 6.4
Re = 83.9

(B) $^2[Re(LH)L_2]^0$ ΔG = 0.0

S = 1/2	
Re-S1	2.51
Re-S2	2.44
Re-S3	2.47
Re-P1	2.47
Re-P2	2.46
Re-P3	2.42
S3-H43	1.38
S2-H44	N/A
P2-Re-P3	169.0

(B) Atom SD %
S1 = 8.6
S2 = 9.1
S3 = 1.1
Re = 76.9

(C) $^2[Re(LH)_2L]^+$ ΔG = 0.0

S = 1/2	
Re-S1	2.38
Re-S2	2.53
Re-S3	2.52
Re-P1	2.40
Re-P2	2.48
Re-P3	2.48
S3-H43	1.38
S2-H44	1.38
P2-Re-P3	167.2

(C) Atom SD %
S1 = 23.1
S2 = 0.0
S3 = 0.0
Re = 70.9

Figure 8. Bond lengths (Å), bond angles (deg), and spin-density percentage contributions for the $S = {}^1/_2$ DFT optimizations (M06/LANL2DZ) of (a) $[ReL_3]^-$, (b) $[Re(LH)L_2]^0$, and (c) $[Re(LH)_2L]^+$.

DOI: 10.1021/acs.inorgchem.6b02829
Inorg. Chem. 2017, 56, 2177−2187

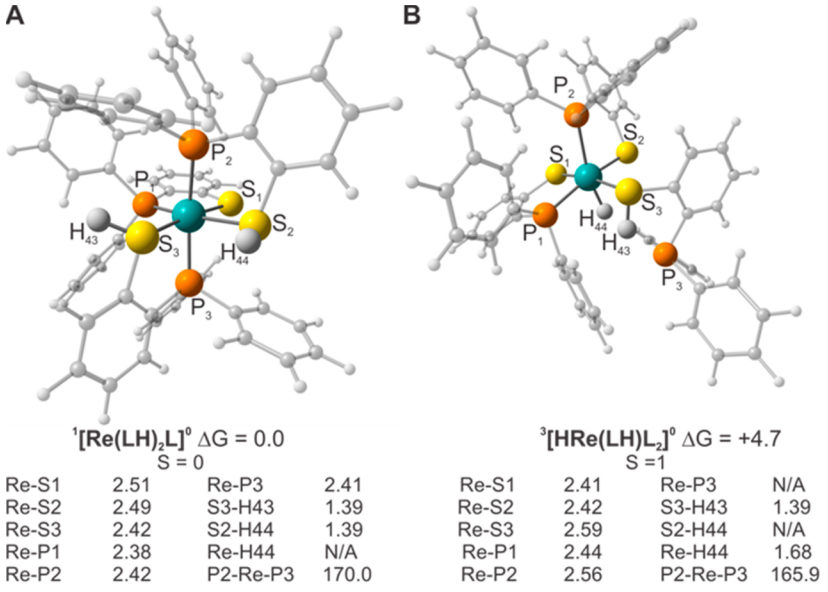

Figure 9. Bond lengths (Å) and angles (deg) for optimizations (M06/LANL2DZ) of (a) $[Re(LH)_2L]^0$ (S = 0) DFT, (b) $[HRe(LH)L_2]^0$ (S = 1), and (c) $[Re(LH)_2L]^+$. ΔG indicates relative zero-point free energy (kcal/mol) values of the S = 0 and S = 1 electronic states.

innocent character. The distance drops from 2.57 Å in $[ReL_3]^-$ to 2.51 Å in $[Re(LH)L_2]$ after initial protonation at S3 with a further decrease to 2.38 Å in $[Re(LH)_2L]^+$ after the second protonation at S2. The Re−S2 bond distance decrease upon protonation at S3 is consistent with an increased SD, which further increases when S2 is protonated. The Re−S3 bond distance shows an increase with each protonation step.

The final step of the HER mechanism is the addition of a second electron to yield the hydrogen evolving complex $ReL_3 \cdot H_2$, which can be represented as either a Re(I)-dithiol or a Re(III)-hydride. The electronic and geometric parameters of the Re(I)-dithiol $[Re(LH)_2L]$ were examined in the singlet (S = 0) as well as the triplet (S = 1) states with only successful optimization of the singlet electronic state, however. The electronic and geometric parameters of the Re(III)-hydride $[HRe(LH)L_2]$ were examined as a singlet (S = 0) and triplet (S = 1) with the triplet being 2.03 kcal/mol lower in energy than the singlet (see Supporting Information). The singlet Re(I)-dithiol (S = 0) configuration is favored over the triplet Re(III)-hydride (S = 1) by 4.7 kcal/mol (Figure 9). This energy gap is sufficiently small, and it should be noted that $[HRe(LH)L_2]$ cannot completely be excluded as the H_2-evolving complex based solely on single point energy calculations.

To unequivocally resolve the electronic structure of the H_2-evolving complex, TS for reaction pathways were located for both $[Re(LH)_2L]$ (Figure 10A) and $[HRe(LH)L_2]$ (Figure 10B). The traditional metal hydride $[HRe(LH)L_2]$ pathway proceeding through TS-$[HRe(LH)L_2]$ requires an insurmountable 81.5 kcal/mol barrier. In contrast, ligand-centered H_2 evolution along the $[Re(LH)_2L]$ pathway proceeds through TS-$[Re(LH)_2L]$ over a modest barrier of 2 kcal/mol (Figure 10C), represented by the imaginary frequency i1113 cm^{-1}. The S−H bond lengths in TS-$[Re(LH)_2L]$, 1.524 and 1.532 Å, are 0.125−0.133 Å longer than the respective equilibrium bond lengths 1.399 and 1.399 Å in $[Re(LH)_2L]$. This may be attributed to a transfer of charge densities from the formal Re(I) to the thiol sulfurs moving forward along the IRC, initiating the release of two H atoms that couple to form hydrogen (see Supporting Information). The IRC analysis is

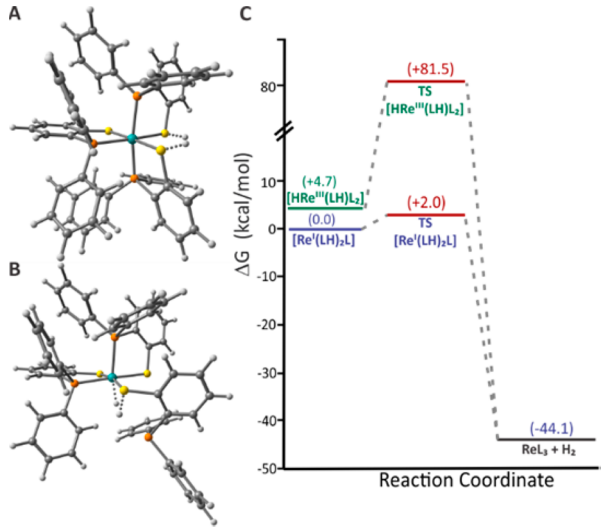

Figure 10. Transition states and energy profile for HER through Re-dithiol and Re-hydride pathways. (A) Representation of TS-[Re-(LH)$_2$L] showing lengthening of two S−H bonds associated with H_2 evolution. (B) Representation of TS-[HRe(LH)L$_2$] showing H_2 evolution from Re−H and S−H. (C) Comparison of relative energies (ZPE corrected) for Re-dithiol and Re-hydride HER pathways using M06/LANL2DZ.

consistent with a ligand-centered H_2 evolution pathway best described as homolytic cleavage of two cis-coordinated metal thiol S−H bonds.

CONCLUSIONS

In summary, we fabricated a series of modified electrodes to translate the nonaqueous, homogeneous HER activity of ReL_3 to a solid support for heterogeneous application in an acidic aqueous environment. The GC-$[ReL_3]$ and GC-$[ReL_3]^+$ electrodes demonstrate good, long-term stability in over-potential following an initial conditioning period. The over-potential can be significantly decreased in freshly prepared

DOI: 10.1021/acs.inorgchem.6b02829
Inorg. Chem. 2017, 56, 2177−2187

electrodes by incorporation of CB, but after conditioning for 1.5 h, the improvement in overpotential is diminished.

Although the relatively large overpotential of these electrodes limits their practical application, the ligand-centered HER by ReL_3 opens the door to novel scaffolds and strategies for catalytic HER development. Furthermore, these electrodes represent a rare example of a well-characterized homogeneous catalyst translated to a heterogeneous surface by simple physisorption. We propose that these catalysts remain intact on the surface as the active HER species but cannot rule out the presence of an undetected quantity of catalytically active degradation products. The remarkable features of this system include long-term stability without inclusion of covalent linkers to the surface, and the proposed translation of both activity and mechanism across homo- and heterogeneous environments.

The metal−thiolate modified electrodes serve as a proxy for a traditional heterogeneous metal surface. All bond-making and bond-breaking is proposed to occur at the sulfur-ligands with the electrode surface providing reducing equivalents without impacting reactivity. The localization of reactivity on the cis-sulfur sites is analogous to the proposed sulfur-edge active site of MoS_2. The strategy of substituting ligand-centered events for reactions on metal surfaces may be also applicable to other molecular catalysts. In this regard, we very recently reported ligand-centered catalytic HER with zinc- and metal-free complexes involving the coupling of N−H bonds.[55] Preparation and evaluation of modified electrodes based on these and related systems is ongoing.

■ ASSOCIATED CONTENT

Supporting Information

The Supporting Information is available free of charge on the ACS Publications website at DOI: 10.1021/acs.inorgchem.6b02829.

Nyquist plots, SEM images after HER catalysis, stability measurement data, optimized geometric parameters of $[HRe(LH)L_2]^0$, intrinsic reaction coordinate analyses, and computational input coordinates (PDF)

■ AUTHOR INFORMATION

Corresponding Authors

*E-mail: robert.buchanan@louisville.edu.

*E-mail: grapperhaus@louisville.edu.

ORCID

Craig A. Grapperhaus: 0000-0003-4889-2645

Author Contributions

⊥W.Z. and A.Z.H. contributed equally.

Notes

The authors declare no competing financial interest.

■ ACKNOWLEDGMENTS

This research was supported in part by the National Science Foundation (Grant CHE-1361728) and a grant from the Kentucky Science and Engineering Foundation pursuant to Grant Agreement KSEF-148-502-15-350 with the Kentucky Science and Technology Corporation. The authors are thankful to Cardinal Research Cluster at the University of Louisville for providing the computational facilities. We thank Xiaoming Fan for help with SEM and Samuel Dilip for help with TEM. We also want to thank Dr. Frank P. Zamborini's lab for usage of the UV-3600 Shimadzu UV−vis−NIR spectrophotometer and a CHI 660 electrochemical workstation and the University of Louisville Conn Center for Renewable Energy Research for providing access to facilities.

■ REFERENCES

(1) Lewis, N. S.; Nocera, D. G. Powering the planet: Chemical challenges in solar energy utilization. *Proc. Natl. Acad. Sci. U. S. A.* **2006**, *103*, 15729−15735.

(2) Turner, J. A. Sustainable hydrogen production. *Science* **2004**, *305*, 972−974.

(3) Gray, H. B. Powering the planet with solar fuel. *Nat. Chem.* **2009**, *1*, 7−7.

(4) Das, A.; Han, Z. J.; Brennessel, W. W.; Holland, P. L.; Eisenberg, R. Nickel Complexes for Robust Light-Driven and Electrocatalytic Hydrogen Production from Water. *ACS Catal.* **2015**, *5*, 1397−1406.

(5) Dubois, M. R.; Dubois, D. L. Development of Molecular Electrocatalysts for CO_2 Reduction and H_2 Production/Oxidation. *Acc. Chem. Res.* **2009**, *42*, 1974−1982.

(6) Haddad, A. Z.; Kumar, D.; Sampson, K. O.; Matzner, A. M.; Mashuta, M. S.; Grapperhaus, C. A. Proposed Ligand-Centered Electrocatalytic Hydrogen Evolution and Hydrogen Oxidation at a Noninnocent Mononuclear Metal-Thiolate. *J. Am. Chem. Soc.* **2015**, *137*, 9238−9241.

(7) Hu, X. L.; Brunschwig, B. S.; Peters, J. C. Electrocatalytic hydrogen evolution at low overpotentials by cobalt macrocyclic glyoxime and tetraimine complexes. *J. Am. Chem. Soc.* **2007**, *129*, 8988−8998.

(8) McNamara, W. R.; Han, Z. J.; Alperin, P. J.; Brennessel, W. W.; Holland, P. L.; Eisenberg, R. A Cobalt-Dithiolene Complex for the Photocatalytic and Electrocatalytic Reduction of Protons. *J. Am. Chem. Soc.* **2011**, *133*, 15368−15371.

(9) McNamara, W. R.; Han, Z. J.; Yin, C. J.; Brennessel, W. W.; Holland, P. L.; Eisenberg, R. Cobalt-dithiolene complexes for the photocatalytic and electrocatalytic reduction of protons in aqueous solutions. *Proc. Natl. Acad. Sci. U. S. A.* **2012**, *109*, 15594−15599.

(10) Smith, S. E.; Yang, J. Y.; DuBois, D. L.; Bullock, R. M. Reversible Electrocatalytic Production and Oxidation of Hydrogen at Low Overpotentials by a Functional Hydrogenase Mimic. *Angew. Chem., Int. Ed.* **2012**, *51*, 3152−3155.

(11) Wiese, S.; Kilgore, U. J.; DuBois, D. L.; Bullock, R. M. $[Ni((P_2N_2Ph)\text{-}N\text{-}Me)_2](BF_4)_2$ as an Electrocatalyst for H_2 Production. *ACS Catal.* **2012**, *2*, 720−727.

(12) Dempsey, J. L.; Brunschwig, B. S.; Winkler, J. R.; Gray, H. B. Hydrogen Evolution Catalyzed by Cobaloximes. *Acc. Chem. Res.* **2009**, *42*, 1995−2004.

(13) McKone, J. R.; Lewis, N. S.; Gray, H. B. Will Solar-Driven Water-Splitting Devices See the Light of Day? *Chem. Mater.* **2014**, *26*, 407−414.

(14) Shaner, M. R.; Atwater, H. A.; Lewis, N. S.; McFarland, E. W. A comparative technoeconomic analysis of renewable hydrogen production using solar energy. *Energy Environ. Sci.* **2016**, *9*, 2354−2371.

(15) Zhang, W.; Lai, W.; Cao, R. Energy-Related Small Molecule Activation Reactions: Oxygen Reduction and Hydrogen and Oxygen Evolution Reactions Catalyzed by Porphyrin- and Corrole-Based Systems. *Chem. Rev.* **2016**, DOI: 10.1021/acs.chemrev.6b00299.

(16) Faber, M. S.; Jin, S. Earth-abundant inorganic electrocatalysts and their nanostructures for energy conversion applications. *Energy Environ. Sci.* **2014**, *7*, 3519−3542.

(17) Popczun, E. J.; Read, C. G.; Roske, C. W.; Lewis, N. S.; Schaak, R. E. Highly Active Electrocatalysis of the Hydrogen Evolution Reaction by Cobalt Phosphide Nanoparticles. *Angew. Chem., Int. Ed.* **2014**, *53*, 5427−5430.

(18) Popczun, E. J.; McKone, J. R.; Read, C. G.; Biacchi, A. J.; Wiltrout, A. M.; Lewis, N. S.; Schaak, R. E. Nanostructured Nickel Phosphide as an Electrocatalyst for the Hydrogen Evolution Reaction. *J. Am. Chem. Soc.* **2013**, *135*, 9267−9270.

DOI: 10.1021/acs.inorgchem.6b02829
Inorg. Chem. 2017, 56, 2177−2187

(19) Kong, D.; Cha, J. J.; Wang, H.; Lee, H. R.; Cui, Y. First-row transition metal dichalcogenide catalysts for hydrogen evolution reaction. *Energy Environ. Sci.* **2013**, *6*, 3553−3558.
(20) Merki, D.; Vrubel, H.; Rovelli, L.; Fierro, S.; Hu, X. L. Fe, Co, and Ni ions promote the catalytic activity of amorphous molybdenum sulfide films for hydrogen evolution. *Chem. Sci.* **2012**, *3*, 2515−2525.
(21) Xiao, P.; Sk, M. A.; Thia, L.; Ge, X. M.; Lim, R. J.; Wang, J. Y.; Lim, K. H.; Wang, X. Molybdenum phosphide as an efficient electrocatalyst for the hydrogen evolution reaction. *Energy Environ. Sci.* **2014**, *7*, 2624−2629.
(22) Jaramillo, T. F.; Jorgensen, K. P.; Bonde, J.; Nielsen, J. H.; Horch, S.; Chorkendorff, I. Identification of active edge sites for electrochemical H_2 evolution from MoS_2 nanocatalysts. *Science* **2007**, *317*, 100−102.
(23) McCrory, C. C. L.; Jung, S.; Ferrer, I. M.; Chatman, S. M.; Peters, J. C.; Jaramillo, T. F. Benchmarking Hydrogen Evolving Reaction and Oxygen Evolving Reaction Electrocatalysts for Solar Water Splitting Devices. *J. Am. Chem. Soc.* **2015**, *137*, 4347−4357.
(24) Zarkadoulas, A.; Field, M. J.; Papatriantafyllopoulou, C.; Fize, J.; Artero, V.; Mitsopoulou, C. A. Experimental and Theoretical Insight into Electrocatalytic Hydrogen Evolution with Nickel Bis(aryldithiolene) Complexes as Catalysts. *Inorg. Chem.* **2016**, *55*, 432−444.
(25) Osmanbas, O. A.; Koca, A.; Kandaz, M.; Karaca, F. Electrocatalytic activity of phthalocyanines bearing thiophenes for hydrogen production from water. *Int. J. Hydrogen Energy* **2008**, *33*, 3281−3288.
(26) Liu, Y. H.; Zhao, J. B.; Li, Z. K.; Mu, C.; Ma, W.; Hu, H. W.; Jiang, K.; Lin, H. R.; Ade, H.; Yan, H. Aggregation and morphology control enables multiple cases of high-efficiency polymer solar cells. *Nat. Commun.* **2014**, *5*, 5293.
(27) Solis, B. H.; Maher, A. G.; Dogutan, D. K.; Nocera, D. G.; Hammes-Schiffer, S. Nickel phlorin intermediate formed by proton-coupled electron transfer in hydrogen evolution mechanism. *Proc. Natl. Acad. Sci. U. S. A.* **2016**, *113*, 485−492.
(28) Le Goff, A.; Artero, V.; Jousselme, B.; Tran, P. D.; Guillet, N.; Metaye, R.; Fihri, A.; Palacin, S.; Fontecave, M. From Hydrogenases to Noble Metal-Free Catalytic Nanomaterials for H_2 Production and Uptake. *Science* **2009**, *326*, 1384−1387.
(29) Pantani, O.; Anxolabehere-Mallart, E.; Aukauloo, A.; Millet, P. Electroactivity of cobalt and nickel glyoximes with regard to the electro-reduction of protons into molecular hydrogen in acidic media. *Electrochem. Commun.* **2007**, *9*, 54−58.
(30) Berben, L. A.; Peters, J. C. Hydrogen evolution by cobalt tetraimine catalysts adsorbed on electrode surfaces. *Chem. Commun.* **2010**, *46*, 398−400.
(31) Lei, H.; Han, A.; Li, F.; Zhang, M.; Han, Y.; Du, P.; Lai, W.; Cao, R. Electrochemical, spectroscopic and theoretical studies of a simple bifunctional cobalt corrole catalyst for oxygen evolution and hydrogen production. *Phys. Chem. Chem. Phys.* **2014**, *16*, 1883−1893.
(32) Mondal, B.; Sengupta, K.; Rana, A.; Mahammed, A.; Botoshansky, M.; Dey, S. G.; Gross, Z.; Dey, A. Cobalt Corrole Catalyst for Efficient Hydrogen Evolution Reaction from H_2O under Ambient Conditions: Reactivity, Spectroscopy, and Density Functional Theory Calculations. *Inorg. Chem.* **2013**, *52*, 3381−3387.
(33) Eady, S. C.; MacInnes, M. M.; Lehnert, N. A Smorgasbord of Carbon: Electrochemical Analysis of Cobalt−Bis(benzenedithiolate) Complex Adsorption and Electrocatalytic Activity on Diverse Graphitic Supports. *ACS Appl. Mater. Interfaces* **2016**, *8*, 23624−23634.
(34) Abe, T.; Taguchi, F.; Imaya, H.; Zhao, F.; Zhang, J.; Kaneko, M. Highly active electrocatalysis by cobalt tetraphenylporphyrin incorporated in a nafion membrane for proton reduction. *Polym. Adv. Technol.* **1998**, *9*, 559−562.
(35) Koca, A. Copper phthalocyanine complex as electrocatalyst for hydrogen evolution reaction. *Electrochem. Commun.* **2009**, *11*, 838−841.
(36) Koca, A.; Kalkan, A.; Bayir, Z. A. Electrochemical, In Situ Spectroelectrochemical, In Situ Electrocolorimetric and Electrocatalytic Characterization of Metallophthalocyanines Bearing Four Dioctylaminocarbonyl Biphenyloxy Substituents. *Electroanalysis* **2010**, *22*, 310−319.
(37) Koca, A.; Kalkan, A.; Bayir, Z. A. Electrocatalytic oxygen reduction and hydrogen evolution reactions on phthalocyanine modified electrodes: Electrochemical, in situ spectroelectrochemical, and in situ electrocolorimetric monitoring. *Electrochim. Acta* **2011**, *56*, 5513−5525.
(38) Koca, A. Hydrogen evolution reaction on glassy carbon electrode modified with titanyl phthalocyanines. *Int. J. Hydrogen Energy* **2009**, *34*, 2107−2112.
(39) Grass, V.; Lexa, D.; Saveant, J. M. Electrochemical generation of rhodium porphyrin hydrides. Catalysis of hydrogen evolution. *J. Am. Chem. Soc.* **1997**, *119*, 7526−7532.
(40) Dilworth, J. R.; Hutson, A. J.; Morton, S.; Harman, M.; Hursthouse, M. B.; Zubieta, J.; Archer, C. M.; Kelly, J. D. The Preparation and Electrochemistry of Technetium and Rhenium Complexes of 2-(Diphenylphosphino)Benzenethiol - the Crystal and Molecular-Structures of $[Re(2\text{-}Ph_2PC_6H_4S)_3]$ and $[Tc(2\text{-}Ph_2PC_6H_4S)_3]$. *Polyhedron* **1992**, *11*, 2151−2155.
(41) Chauhan, R.; Moreno, M.; Banda, D. M.; Zamborini, F. P.; Grapperhaus, C. A. Chemiresistive metal-stabilized thiyl radical films as highly selective ethylene sensors. *RSC Adv.* **2014**, *4*, 46787−46790.
(42) Kochowski, S.; Nitsch, K. Description of the frequency behaviour of metal-SiO2-GaAs structure characteristics by electrical equivalent circuit with constant phase element. *Thin Solid Films* **2002**, *415*, 133−137.
(43) Zhao, Y.; Truhlar, D. G. The M06 suite of density functionals for main group thermochemistry, thermochemical kinetics, noncovalent interactions, excited states, and transition elements: two new functionals and systematic testing of four M06-class functionals and 12 other functionals. *Theor. Chem. Acc.* **2008**, *120*, 215−241.
(44) Frisch, M. J.; Trucks, G. W.; Schlegel, H. B.; Scuseria, G. E.; Robb, M. A.; Cheeseman, J. R.; Montgomery, J. A., Jr.; Vreven, T.; Kudin, K. N.; Burant, J. C.; Millam, J. M.; Iyengar, S. S.; et al. *Gaussian 09*, revision A.01; Gaussian, Inc.: Wallingford, CT, 2009.
(45) Becke, A. D. Density-functional thermochemistry. III. The role of exact exchange. *J. Chem. Phys.* **1993**, *98*, 5648−5652.
(46) Lee, C.; Yang, W.; Parr, R. G. Development of the Colle-Salvetti correlation-energy formula into a functional of the electron density. *Phys. Rev. B: Condens. Matter Mater. Phys.* **1988**, *37*, 785−789.
(47) Stephens, P. J.; Devlin, F. J.; Chabalowski, C. F.; Frisch, M. J. Ab Initio Calculation of Vibrational Absorption and Circular Dichroism Spectra Using Density Functional Force Fields. *J. Phys. Chem.* **1994**, *98*, 11623−11627.
(48) Vosko, S. H.; Wilk, L.; Nusair, M. Accurate spin-dependent electron liquid correlation energies for local spin density calculations: a critical analysis. *Can. J. Phys.* **1980**, *58*, 1200−1211.
(49) Grapperhaus, C. A.; Kozlowski, P. M.; Kumar, D.; Frye, H. N.; Venna, K. B.; Poturovic, S. Singlet diradical character of an oxidized ruthenium trithiolate: electronic structure and reactivity. *Angew. Chem., Int. Ed.* **2007**, *46*, 4085−4088.
(50) Andrienko, G. *ChemCraft*. http://www.chemcraftprog.com. (Accessed January, 2017).
(51) Grapperhaus, C. A.; Ouch, K.; Mashuta, M. S. Redox-regulated ethylene binding to a rhenium-thiolate complex. *J. Am. Chem. Soc.* **2009**, *131*, 64−65.
(52) Huang, Z. J.; Luo, W. J.; Ma, L.; Yu, M. Z.; Ren, X. D.; He, M. F.; Polen, S.; Click, K.; Garrett, B.; Lu, J.; Amine, K.; Hadad, C.; Chen, W. L.; Asthagiri, A.; Wu, Y. Y. Dimeric $[Mo_2S_{12}]^{2-}$ Cluster: A Molecular Analogue of MoS_2 Edges for Superior Hydrogen-Evolution Electrocatalysis. *Angew. Chem., Int. Ed.* **2015**, *54*, 15181−15185.
(53) Chen, Z. B.; Cummins, D.; Reinecke, B. N.; Clark, E.; Sunkara, M. K.; Jaramillo, T. F. Core-shell MoO_3-MoS_2 Nanowires for Hydrogen Evolution: A Functional Design for Electrocatalytic Materials. *Nano Lett.* **2011**, *11*, 4168−4175.
(54) Thomas, J. G. *Trans. Faraday Soc.* **1961**, *57*, 1603−1611.
(55) Haddad, A. Z.; Garabato, B. D.; Kozlowski, P. M.; Buchanan, R. M.; Grapperhaus, C. A. Beyond Metal-Hydrides: Non-Transition-

DOI: 10.1021/acs.inorgchem.6b02829
Inorg. Chem. 2017, 56, 2177−2187

Metal and Metal-Free Ligand-Centered Electrocatalytic Hydrogen Evolution and Hydrogen Oxidation. *J. Am. Chem. Soc.* **2016**, *138*, 7844−7847.

DOI: 10.1021/acs.inorgchem.6b02829
Inorg. Chem. 2017, 56, 2177−2187